remote sensing

MDPI

Article

Observation of Boundary-Layer Jets in the Northern South China Sea by a Research Vessel

Xiyun Zhang [1,2,3,†], Yuhan Luo [1,2,3,†] and Yu Du [1,2,3,*]

[1] School of Atmospheric Sciences, Sun Yat-sen University, and Southern Marine Science and Engineering Guangdong Laboratory (Zhuhai), Zhuhai 519082, China; zhangxy739@mail2.sysu.edu.cn (X.Z.); luoyh23@mail2.sysu.edu.cn (Y.L.)
[2] Guangdong Province Key Laboratory for Climate Change and Natural Disaster Studies, Sun Yat-sen University, Zhuhai 519082, China
[3] Key Laboratory of Tropical Atmosphere-Ocean System (Sun Yat-sen University), Ministry of Education, Zhuhai 519082, China
* Correspondence: duyu7@mail.sysu.edu.cn; Tel.: +86-138-0243-8346
† These authors contributed equally to this work.

Abstract: Boundary-layer jets (BLJs) in the South China Sea play an important role in heavy rainfall in South China, yet observations in maritime locations are still limited. This study examines the vertical structures and temporal evolutions of BLJs in the northern South China Sea using intensive radiosonde observations from a research vessel from 15 to 18 June 2022 and evaluates the performance of various reanalysis datasets in capturing these features. Observations identified BLJs with jet cores at altitudes of approximately 500–700 m. Wind speeds slightly decreased from 15 to 16 June and then significantly increased after 17 June, showing double peaks on 17 June below 1 km at altitudes of 250 and 700 m. Among the reanalysis datasets, ERA5 exhibited more accurate results on average, followed by MERRA2, both of which outperformed JRA55 and FNL. ERA5 and MERRA2 had mixed performances in depicting BLJ characteristics. ERA5 accurately captured the initial decrease in wind speeds and their subsequent enhancement, while MERRA2 initially faltered but improved later. On the diurnal scale, neither MERRA2 nor ERA5 accurately represented the wind speed peaks observed at 2300 and 1100 LST, whereas ERA5 roughly reflected the nocturnal acceleration of the BLJs. During the observation period, the intensification of BLJs in the northern SCS, influenced by an eastward-moving high-pressure system and a southward-moving low-pressure vortex, led to enhanced precipitation in South China that gradually moved northward from the coastline to inland regions. This study provides new insights into the detailed characteristics of marine BLJs based on direct observations.

Keywords: boundary-layer jets; shipboard observations; performance of reanalysis datasets

Citation: Zhang, X.; Luo, Y.; Du, Y. Observation of Boundary-Layer Jets in the Northern South China Sea by a Research Vessel. *Remote Sens.* **2024**, *16*, 3872. https://doi.org/10.3390/rs16203872

Academic Editor: Sang-Hyun Lee

Received: 29 August 2024
Revised: 12 October 2024
Accepted: 16 October 2024
Published: 18 October 2024

1. Introduction

A low-level jet (LLJ) is an important weather phenomenon with notable impacts globally [1,2]. LLJs play crucial roles in influencing rainfall by creating favorable conditions for convective activities through both thermodynamic and dynamic processes [1–3]. Thermodynamically, LLJs transport warm and moist air, destabilizing the lower atmosphere [4,5]. The intensity of LLJs directly affects the transport and convergence of water vapor [2,4–6]. Dynamically, the convergence at the terminus of LLJs enhances upward motions, thus promoting convection [4,7,8].

In South China, LLJs occur frequently in early summer. An LLJ is generally defined by the following criteria: (1) the maximum wind speed below 700 hPa exceeds 10 m s^{-1}, and (2) there is a strong vertical wind shear, characterized by a wind speed decrease of at least 3 m s^{-1} in wind speed from the maximum to the next minimum at or below the 600 hPa level. Building on this definition, LLJs can be classified into two main types based on their

different characteristics and formation mechanisms [9–12]: (1) the boundary layer jet (BLJ), which occurs below 1 km and exhibits profound diurnal variation, and (2) the synoptic-weather-related LLJ (SLLJ), with its core located at higher altitude (~850–700 hPa). Both types are crucial for rainfall in South China [2,13,14]. Unlike SLLJs, which are predominantly observed over the inland of South China, BLJs exhibit a higher frequency over the Beibu Gulf and the northern South China Sea (SCS) [2,15,16]. Based on a reanalysis dataset, Du et al. [16] identified that the BLJ cores over the northern SCS are primarily located at 950 hPa, with their peak occurrences in June. Numerical models suggest that BLJs over the northern SCS facilitate convection initiation and subsequent upscale convective growth along the South China coast [17]. Dong et al. [15] also utilized a reanalysis dataset and documented that BLJs over the northern SCS impact afternoon rainfall in inland Guangdong Province due to their influence on dynamic lifting and moisture transport.

BLJs are affected by both synoptic weather systems and boundary processes. On the synoptic scale, a persistent pressure gradient force aids in maintaining the BLJ [18–20]. On the diurnal scale, the formation of the BLJ with a nighttime peak is explained by mechanisms such as inertial oscillation theory [21,22], baroclinic theory related to topographic thermal difference [22,23], or a combination of these factors [18,24,25].

Despite advances in understanding BLJs, most observational research in China has focused on inland regions [10,19,26,27]. For instance, Cui et al. [27] documented that BLJs in the middle reaches of the Yangtze River concentrate between 300–1200 m and typically peak at 2300 LST based on radiosonde data. Miao et al. [19] compared the characteristics of LLJs in Beijing and Guangzhou using wind profiler data and soundings. Yan et al. [26] examined the strengths, heights, and wind directions of LLJs in inland China using long-term radiosonde observations.

Numerous studies have documented the characteristics of coastal BLJs across various regions of the world. For instance, Holt and Sethuraman [28] confirmed the existence of a BLJ, known as Somali Jet, with its core near 900 hPa and wind speeds exceeding 16 m s^{-1}, based on aircraft and ship-launched radiosondes. In the Antarctica region, Andreas et al. [29] documented the frequent occurrence of BLJs at the Ice Station Weddell, with jet cores primarily below 400 m and a wind speed of less than 14 m s^{-1}, using radiosonde data. Over the Arctic Ocean, Jakobson et al. [30] utilized observations from the drifting ice station Tera to investigate the characteristics of BLJs, identifying jet cores below 1200 m with a wind speed of less than 12 m s^{-1}. Specifically, BLJs in the northern SCS, located upstream of South China, are critical for improving precipitation predictions in South China, possibly through assimilating their observations. However, due to limited observational data over the northern SCS, the characteristics and structures of BLJs remain inadequately verified through observations.

Previous studies over the northern SCS (15°N–22°N, 110°E–121°E) have primarily utilized reanalysis datasets and numerical models to explore the characteristics of BLJs, highlighting the need for performance evaluation of these datasets. ERA5 generally aligns closely with observations [27,31–34]. In the North Sea, ERA5 has shown biases in wind speed representation and poor one-to-one correspondence for LLJs relative to met-mast and lidar observations, though it captures climatological characteristics effectively, including seasonal cycles and circulation patterns [34]. Similarly, in the southern Baltic Sea, ERA5 underestimates LLJ occurrences and struggles with core height and shear representation compared to ship-based lidar measurements [31]. MERRA2 tends to overestimate near-surface wind speeds, while JRA-55 underestimates them [32]. Given these reanalysis datasets' varied performances in different regions and conditions, it is crucial to assess their accuracy for BLJs in the northern SCS.

From 15 to 18 June 2022, the Sun Yat-sen University research vessel conducted its maiden voyage for scientific expedition in the northern SCS, which coincided with the BLJ events. Radiosonde-equipped sounding balloons were launched up to eight times in a single day during the study period to measure wind speeds, temperature, pressure, and humidity. These radiosondes provided high vertical resolution (approximately 100 m

in the lower levels below 2 km) up to 25 km, offering critical data for studying BLJs' characteristics and temporal evolution. This leads to several scientific questions: (1) What are the observed characteristics of BLJs in the northern SCS, their variation mechanisms, and their relationships with precipitation? (2) How accurately do reanalysis datasets capture the vertical structure and temporal evolution of BLJs in the northern SCS during this period?

Therefore, this study aims to examine BLJs in the northern SCS through radiosonde observations and to evaluate the performance of reanalysis datasets. The following section outlines the data and methodology, including an overview of radiosonde data during the expedition. Section 3 analyzes the observed characteristics of BLJs, while Section 4 compares observational and reanalysis datasets. The mechanisms driving BLJ variations and their relationship with precipitation are described in Section 5. The final section summarizes the results.

2. Data and Methodology

2.1. Data

From 15 to 18 June 2022, a scientific expedition was conducted in the northern SCS by the Sun Yat-sen University research vessel on its maiden voyage (Figure 1a). This study utilized data obtained from radiosonde-equipped sounding balloons, which were released on the deck (Figure 1b). The vessel navigated between 112°E~113.5°E and 16.5°N~21.5°N. Figure 1c presents the locations of the vessel from 15 to 18 June, where sounding balloons were launched, and the surrounding terrain.

Sounding balloons were released every six hours from 1400 LST on 15 June to 0800 LST on 16 June and every three hours from 1400 LST on 17 June to 2300 LST on 18 June. These radiosondes measured temperature, pressure, and dew point temperature. In addition, by analyzing the changes in the radiosonde positions over time, wind speeds and directions were calculated. In the process of radiosonde sounding, data availability was ensured by transmitting digital error correction codes via the VAISALA system, and the telemetry error was continuously measured and checked to maintain data quality.

To better compare the temporal evolution of BLJs with reanalysis datasets, the dew point temperature and wind speed data at each observation point were interpolated to 950 hPa.

To investigate the vertical structures, temporal characteristics, associated atmospheric environmental conditions, and influences of BLJs on precipitation during this expedition, the fifth-generation European Centre for Medium-Range Forecasts (ECMWF) atmospheric reanalysis dataset (ERA5) [35] was used, with a horizontal resolution of 0.25° × 0.25°, 37 pressure levels, and a time interval of 1 h. Additionally, three other reanalysis datasets were evaluated for the temporal variation of BLJs during the observation period from 1400 LST on 15 June to 2300 LST on 18 June: (1) National Centers for Environmental Prediction (NCEP) Final Operational Model Global Tropospheric Analyses (FNL) with a horizontal resolution of 1° × 1° (approximately 100 km), 26 pressure levels, and a time interval of 6 h; (2) Japan Meteorological Agency's 55-year reanalysis projects reanalysis (JRA55), with a spatial resolution 0.5625° × 0.5625° and a time interval of 6 h; and (3) Modern-Era Retrospective Analysis for Research and Applications, Version 2 (MERRA2) reanalysis, with a horizontal resolution of 0.5° latitude by 0.625° longitude, 72 vertical layers, and a time interval of 1 h.

The Climate Prediction Center morphing technique (CMORPH) rainfall data with a temporal resolution of 30 min and a horizontal resolution of 8 km × 8 km was also utilized to assess precipitation associated with BLJs during this period.

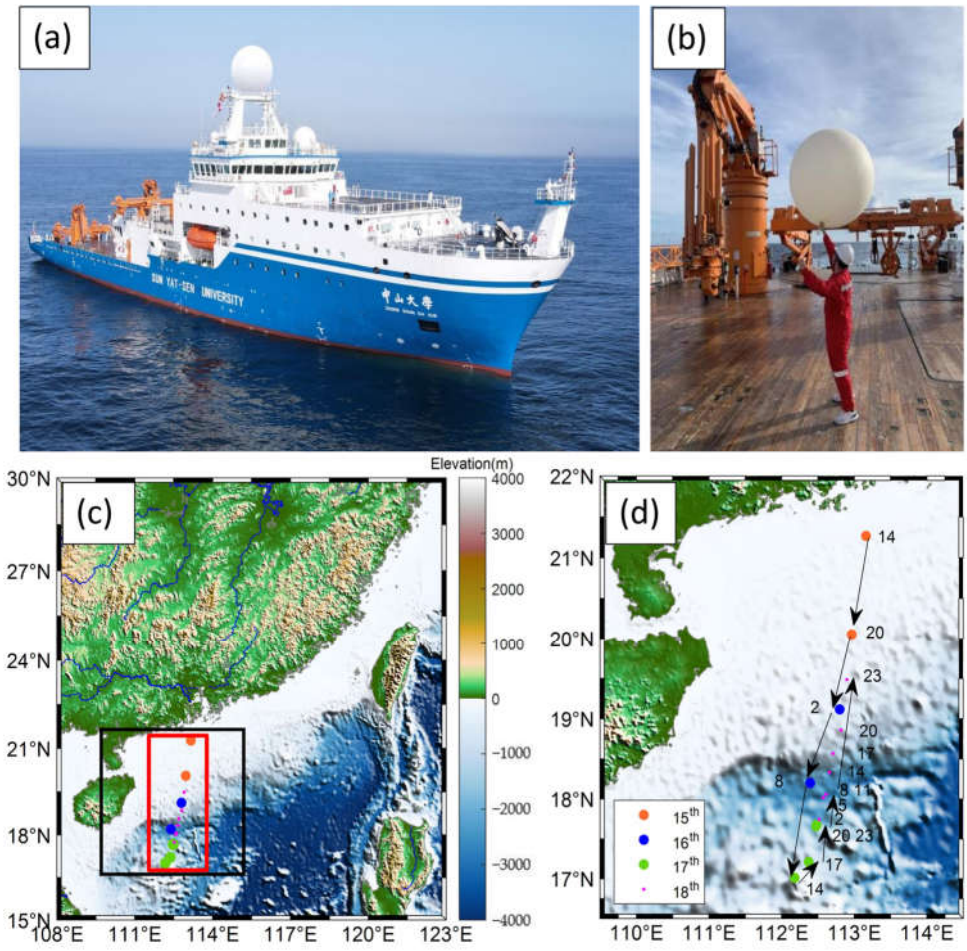

Figure 1. (**a**) A photo of the Sun Yat-sen University Research Vessel. (**b**) Sounding balloon launched during the observation. (**c**) Geographical environment and locations of the research vessel. (**d**) Enlarged view of the area with the black box area in (**c**). The dots in (**c**,**d**) indicate the shipboard observation locations on 15 (orange), 16 (blue), 17 (green), and 18 (magenta) June, with the numbers next to the dots indicating LST at the observational time.

2.2. Methodology

A momentum budget analysis based on ERA5 was conducted to investigate the mechanisms responsible for maintaining the BLJs. Following the approaches of Du et al. [12,16] and Zeng et al. [36], the momentum budget equation can be written as follows:

$$\underbrace{\frac{\partial \boldsymbol{V}}{\partial t}}_{TD} = \underbrace{-\boldsymbol{V}_h \cdot \nabla_h \boldsymbol{V}}_{HAD} \underbrace{-\omega \frac{\partial \boldsymbol{V}}{\partial p}}_{VAD} \underbrace{-\nabla \phi}_{PGF} \underbrace{-f\boldsymbol{k} \times \boldsymbol{V}}_{CF} + \underbrace{\boldsymbol{F}_r}_{F_r}. \quad (1)$$

In this equation, the term on the left-hand side represents the tendency of winds (TD). The terms on the right-hand side correspond to horizontal advection (HAD), vertical advection (VAD), pressure gradient force (PGF), Coriolis force (CF), and friction force (Fr), respectively. Fr is calculated as a residual from other items.

For a quantitative assessment of how accurately four reanalysis datasets represent observations, root mean square error (RMSE) and mean absolute error (MAE) were utilized. Following the methods of Khosravi et al. [37], Maier et al. [38], and Karunasingha et al. [39], the RMSE and MAE are calculated as $\sqrt{\left(\sum_{i=1}^{n}(x_i - \hat{x}_i)^2/n\right)}$ and $\left(\frac{1}{n}\right)\sum_{i=1}^{n}|x_i - \hat{x}_i|$, respectively, where n indicates the number of interpolated data points at each observation, x_i

represents the observed values, and $\hat{x}_i$ represents the corresponding values in reanalysis datasets.

3. Characteristics of BLJs in Observation

This section provides a brief overview of the synoptic atmospheric environment during the observation period, with a focus on the characteristics of BLJs. This section emphasizes the vertical profiles, temporal variations, and associated moisture of BLJs as derived from observational data.

3.1. Synoptic Background

Based on the ERA5 dataset, Figure 2 illustrates the large-scale atmospheric conditions during the research cruise, showing geopotential height at 500 hPa and equivalent potential temperature at 950 hPa, along with the wind field at 950 hPa. The western Pacific subtropical high (WPSH) was located over the northern SCS, as indicated by the westward extension of the 5880 gpm contour. The observation positions of this research cruise were situated at the boundary between the high- and low-pressure systems, coinciding with the BLJs' location over the northern SCS. BLJs in the northern SCS fall within the meso- to synoptic-scale range, extending several hundred kilometers along the jet axis. Regions with high equivalent potential temperatures exceeding 348 K in the northern SCS created favorable thermal conditions, facilitating BLJs in transporting warm, moist air toward South China, which thereby could potentially enhance precipitation.

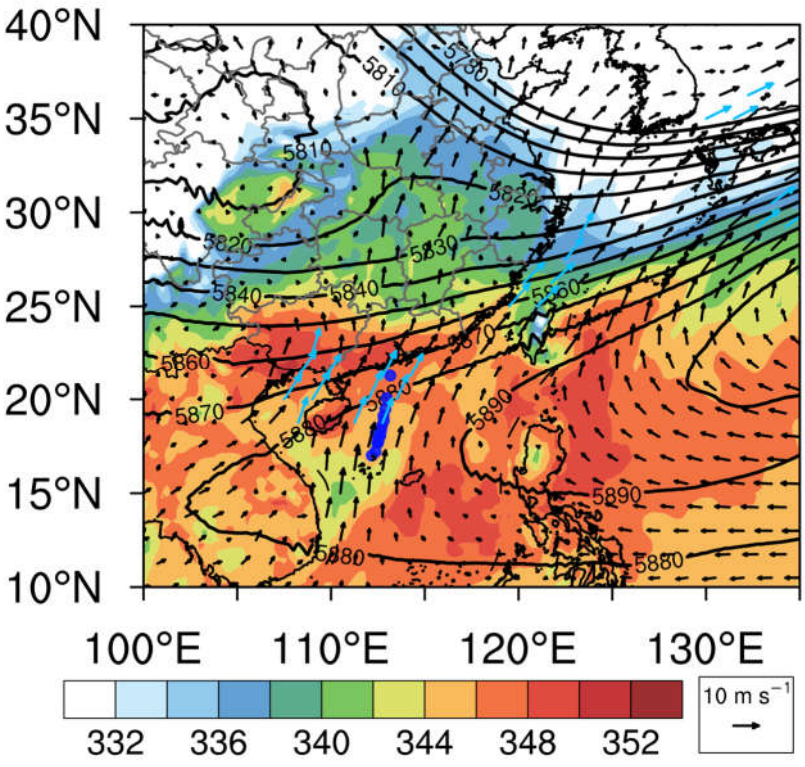

Figure 2. Horizontal distribution of equivalent potential temperature (shading, unit: K) and wind vectors (blue vectors indicate wind speed exceeding 10 m s^{-1}) at 950 hPa superimposed with geopotential height at 500 hPa (black contours, interval = 10 gpm) averaged from 15 to 18 June. The blue dots denote the positions of the research vessel during the observation period.

3.2. Temporal and Vertical Structures of BLJs and Corresponding Moisture

The vertical profiles and temporal variations of wind speeds and directions are depicted in Figure 3 based on radiosonde data during the observational period. These profiles

typically exhibited a BLJ structure, characterized by wind speeds exceeding 10 m s^{-1} and significant wind shears greater than 3 m s^{-1} (Figure 3c,d).

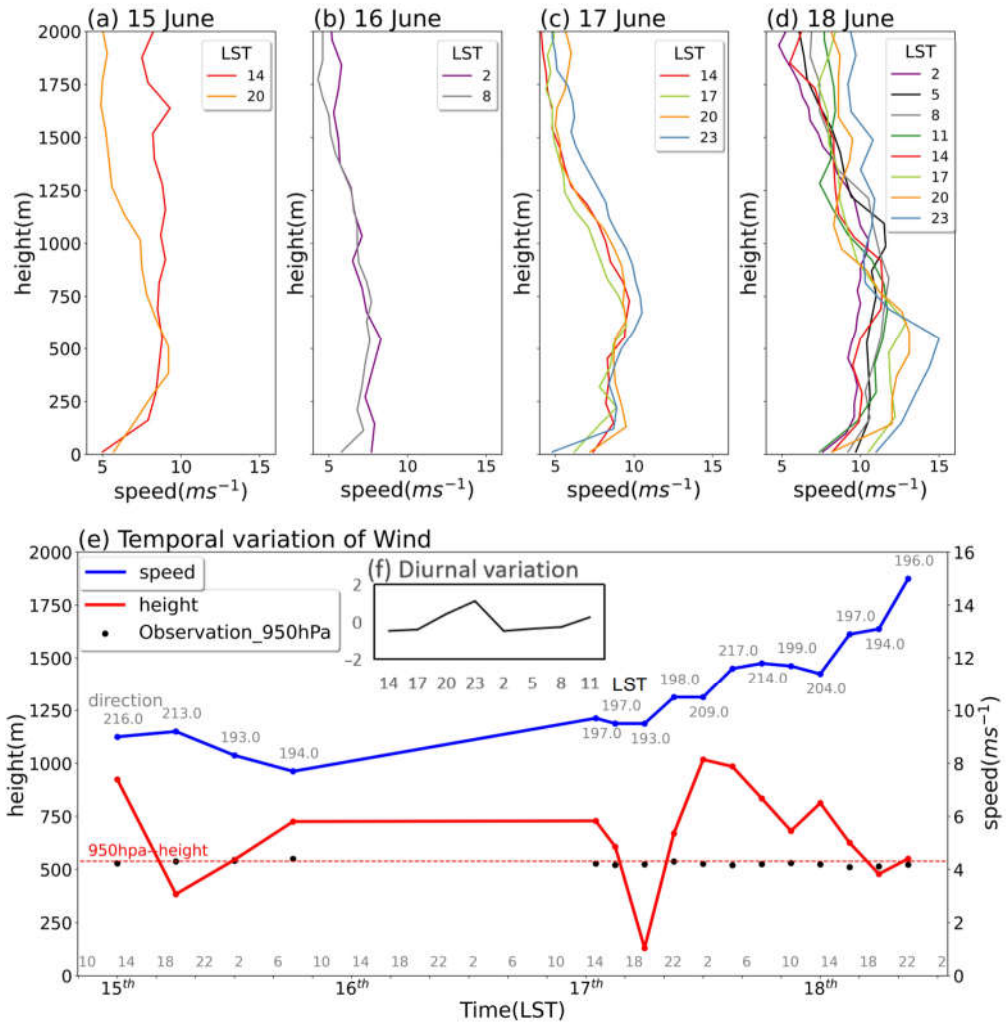

Figure 3. (**a**–**d**) Vertical profiles of wind speed for each day from 15 to 18 June, respectively. (**e**) Temporal evolutions of maximum wind speed (blue line), along with the corresponding wind directions (grey numbers) and altitudes (red line) below 1 km. (**f**) Average diurnal variation of wind speed deviation (m s^{-1}) at 950 hPa. The red dashed line in (**e**) indicates the reference height of 950 hPa, and the black marks represent the actual height of 950 hPa in observation.

At 2000 LST on 15 June, a strong wind shear was observed, with a reduction of more than 3 m s^{-1} from the maximum at 500 m to the minimum at around 1500 m. Additionally, a wind shear greater than 3 m s^{-1} was observed at 0800 LST on 16 June. Despite the lack of corresponding observational data for these time periods, the ERA5 results indicate wind speeds greater than 10 m s^{-1} across a large area of the northern SCS on 16 June. Thus, it can be affirmed that BLJs occurred on 16 June. A slight decrease in wind speeds was observed on 16 June (Figure 3b), likely related to the movement of the research vessel. On 17 June, the wind speed profiles displayed obvious double peaks at altitudes of roughly 250 m and 750 m (Figure 3c). Notably, on 18 June, the BLJ exhibited an enhancement in both wind speed and vertical wind shear compared to other days, with the jet core located around 500 m, wind speed approaching nearly 15 m s^{-1}, and vertical wind shear exceeding 5 m s^{-1} (Figure 3d).

A trend of initial slight low-level wind speeds decrease followed by strengthening was observed on the synoptic scale during the study period, which is consistent with the

vertical wind speed profiles in Figure 3a–d, particularly for the southwesterlies (Figure 3e). The heights of maximum wind speeds consistently remained below 1 km around 950 hPa, while the actual height of 950 hPa showed slight variations during the period. The average diurnal pattern of BLJs in Figure 3f was derived by subtracting their corresponding first-order linear trend to exclude the synoptic-scale impact. On a diurnal scale, wind speeds reached a peak at approximately 2300 LST during nighttime, with a secondary peak around 1100 LST. Similar diurnal variations were also observed in the vertical profiles. On 15 June, a more pronounced vertical wind shear appeared at 2000 LST, with stronger winds at the altitude of 250–500 m compared to 1400 LST, reflecting the potential influence of boundary processes (Figure 3a). On both 17 and 18 June, the maximum wind speeds below 1 km occurred at 2300 LST with a jet core located near 750 and 500 m, respectively (Figure 3c,d).

Dong et al. [15] explored the mechanisms behind the primary peak during the nighttime and the secondary peak in the afternoon. The nocturnal peak is attributed to the inertial oscillation of ageostrophic winds. In the maritime regions, these ageostrophic winds originate from the large-scale land–sea breeze rather than the reduction in frictional force at night as suggested by the traditional Blackadar mechanism [2,15,40]. The afternoon peak is primarily driven by the thermal effects of Hainan Island [15]. On a diurnal scale, solar heating around noon creates a local thermal low over Hainan Island, strengthening the southerly geostrophic wind on the island's eastern side.

Vertical profiles of moisture were examined to understand the significant impact of BLJs on regulating moisture distribution through transport processes [2,15]. The maximum specific humidity was primarily concentrated below 1 km, reaching values close to 20 g kg^{-1} (Figure 4a–d). The altitude at which specific humidity reached 17.5 g kg^{-1} varied throughout the observation period: it decreased from approximately 650 m on 15 June to 500 m on 16 June, then increased from near 400 m on 17 June to 680 m on 18 June, indicating a thickening of the moist layer over time. Correspondingly, specific humidity at 950 hPa exhibited a decrease from 15 to 16 June, followed by a continuous increase after 17 June (Figure 4e). The temporal variation of specific humidity aligned with that of the BLJs, showing an increasing trend on the synoptic scale. This suggests that the BLJs contributed to enhanced moisture fluxes and transport during this period [18,41].

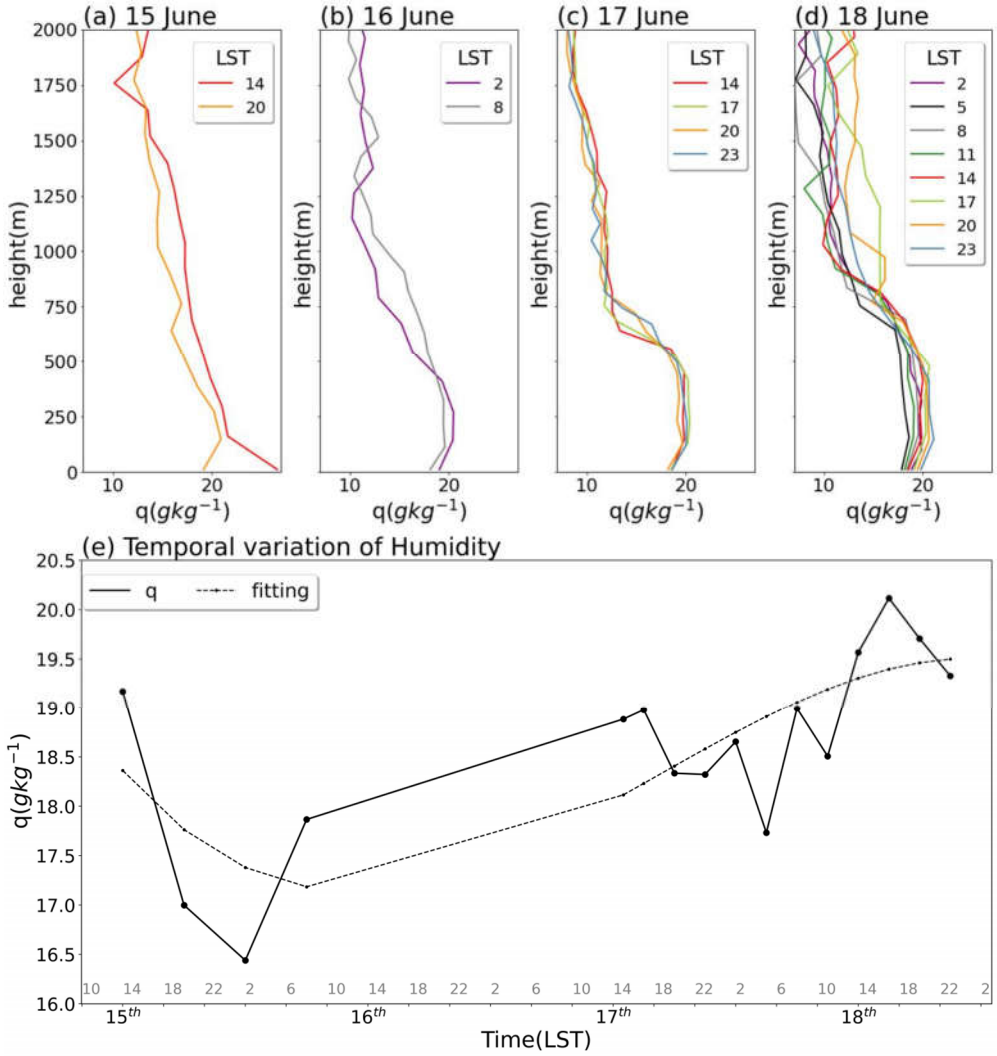

Figure 4. (**a**–**d**) Vertical profiles of specific humidity for each day from 15 to 18 June, respectively. (**e**) Temporal evolution of specific humidity at 950 hPa (black solid line) along with its seventh-order linear trend (black dashed line).

4. Comparison Between Observation and Reanalysis Datasets

In this section, we compare the vertical characteristics and temporal evolutions of BLJs between observational data and reanalysis datasets. Additionally, we perform a quantitative evaluation of errors in the reanalysis datasets.

4.1. Temporal and Vertical Comparisons of Wind and Moisture

The daily average wind speed vertical profiles retrieved from the ERA5 and MERRA2 datasets are compared with the observational data from 15 to 18 June (Figure 5a–d). On 15 June, the wind speeds and vertical wind shears in ERA5 and MERRA2 were insufficiently pronounced, especially at 500 m, failing to adequately represent the BLJ characteristics documented in the observational profiles (Figure 5a). On 16 June, ERA5 exhibited better performance in capturing the general characteristics of the observed atmospheric condition within the altitude range from 0 to 2000 m. In contrast, MERRA2 struggled to capture fine-scale variations in wind speed at different altitudes. On 17 June, the daily average wind speed profile in the observations exhibited double peaks at 250 and 750 m (Figure 5c). However, both ERA5 and MERRA2 failed to capture these two peaks, with the BLJ core height in both datasets being consistently around 500 m, though ERA5 more closely approximated the observed wind speeds below 1 km. On 18 June, both reanalysis datasets

and observational data displayed the BLJ characteristics, with ERA5 exhibiting a closer resemblance to the observed wind speed profile and MERRA2 slightly underestimating it (Figure 5d).

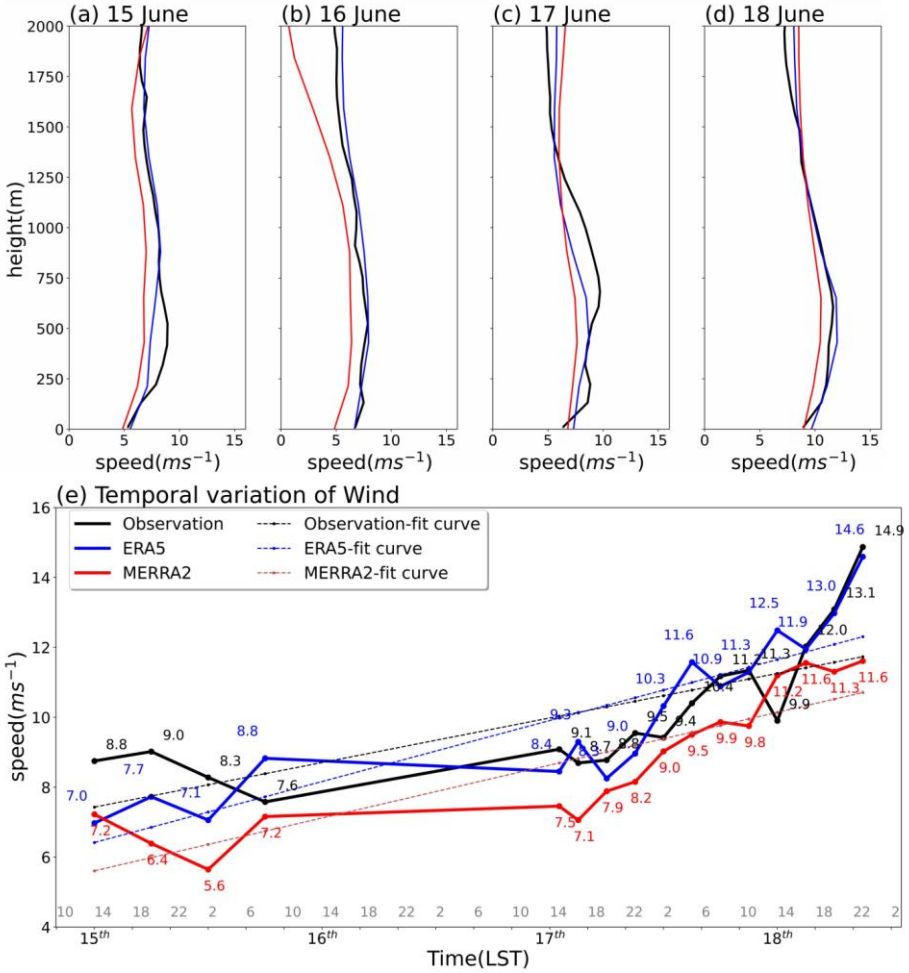

Figure 5. (**a**–**d**) Vertical profiles of daily averaged wind speeds from 15 to 18 June, as retrieved from observational data (black solid lines), the ERA5 dataset (blue solid lines), and the MERRA2 dataset (red solid line). (**e**) Temporal evolution of wind speeds at 950 hPa (solid lines) and their first-order linear trend (dashed lines) based on observational data (black lines), ERA5 (blue lines), and MERRA2 (red lines).

This inability of the reanalysis datasets to accurately represent the detailed vertical structures of BLJs might be attributed to the inadequate horizontal and vertical resolution of the models, as well as limitations in the parameterization of the boundary layer. Different horizontal resolutions in various reanalysis datasets can result in varying degrees of horizontal smoothing, potentially obscuring fine-scale features of BLJs. Moreover, the selection and tuning of boundary layer schemes can significantly impact the representation of turbulence mixing and vertical temperature stratification, both of which are essential processes in the formation and maintenance of BLJs [42].

Figure 5e compares the temporal evolutions of wind speed at approximately 950 hPa near the observation locations from the ERA5 and MERRA2 datasets with the corresponding measured data. Both ERA5 and MERRA2 generally captured the synoptic-scale increase, while MERRA2 underestimated the strength of BLJs slightly. However, the details of their representation differed.

From 15 June to 0200 LST on 16 June, the observation and ERA5 displayed a similar trend, initially with a slight increase followed by a decrease, although ERA5 consistently

underestimated wind speeds by approximately 1 m s^{-1}. Conversely, MERRA2 demonstrated a contrary trend during this period. From 0200 to 0800 LST on 16 June, both ERA5 and MERRA2 showed an increasing trend, while the observations, however, displayed a decreasing trend. The differences among the ERA5, MERRA2, and observational data were relatively small after 1400 LST on 17 June. During this period, compared to MERRA2, ERA5 more accurately captured the pronounced increasing trend in wind speeds recorded in the observational data, whereas MERRA2 generally underestimated the wind speeds by approximately 1 m s^{-1}. This discrepancy might stem from the varying capabilities of the reanalysis datasets to resolve the fine-scale horizontal distributions of the BLJs, as reflected by the shifting comparison points due to the moving observational ship.

Figure 6a compares the temporal evolutions of the specific humidity profiles, averaged along the black line in Figure 6b, between the observational data and the ERA5 dataset. Overall, ERA5 underestimated moisture in the lower layers, particularly at around 950 hPa, where the thickness of moisture exceeding 17.5 g kg^{-1} was underestimated. In contrast, specific humidity was overestimated in mid-levels. For instance, specific humidity below 7.5 g kg^{-1} was observed at 800 hPa during the research campaign, while ERA5 recorded values exceeding 7.5 g kg^{-1} at the same level.

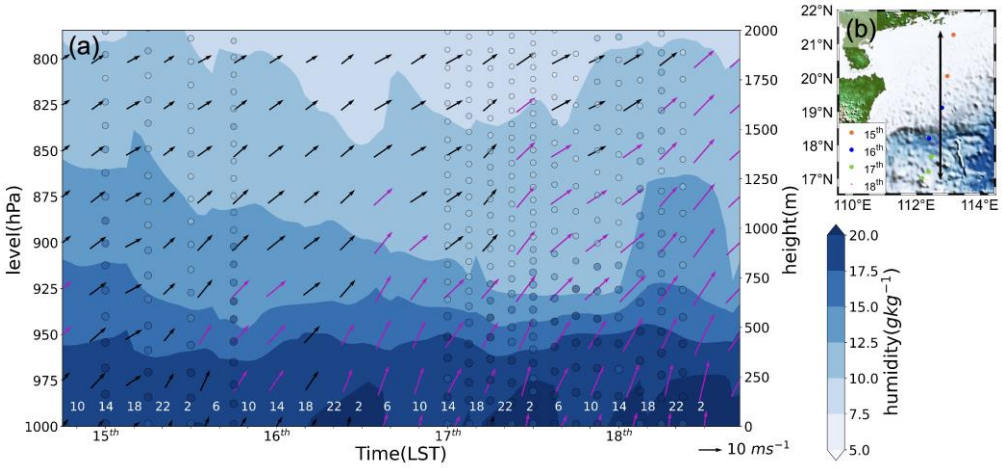

Figure 6. (**a**) Temporal evolution of the specific humidity profiles in ERA5 (shading, g kg^{-1}) and horizontal wind vectors (purple vectors indicate wind speeds greater than 10 m s^{-1}), superimposed with observational specific humidity profiles (colored dots, with both color and size indicating the magnitudes of specific humidity). (**b**) Map with the black line (upper right) defining the cross-section location used in panel (**a**).

The inability of the ERA5 reanalysis dataset to accurately represent specific humidity, typically underestimating it in lower levels of BLJs while overestimating it at higher levels, might be attributed to the vertical resolution of the model. Nevertheless, ERA5 generally captured the observed thickening of the moist layer below 1 km after 17 June, corresponding to enhanced southwesterlies, though some detailed discrepancies were present.

In the observational data, as shown in dots in Figure 6a, the altitude at which the specific humidity reached 12.5 g kg^{-1} showed a significant decreasing trend to 800 m on 15 June and a gradual increase to approximately 1.3 km during 17–18 June, with two minor peaks at 0800 LST on 16 June and 1700 LST on 18 June, respectively. Compared to observations, the thickness of the moist layer in ERA5 did not reflect the first minor peak but demonstrated consistency with observational data after 17 June. The detailed temporal differences between ERA5 and the observational data might be related to the varying positions of shipboard observations.

4.2. Horizontal and Diurnal Variations of BLJs

Figure 7 presents the temporal variation of horizontal wind speed distributions at 950 hPa based on the ERA5 dataset. From 16 to 18 June, regions where wind speeds exceeded 10 m s^{-1}, indicative of BLJs, were observed in the Beibu Gulf and the northern SCS. The observed times, indicated by blue markers, fell within the influence range of these BLJs.

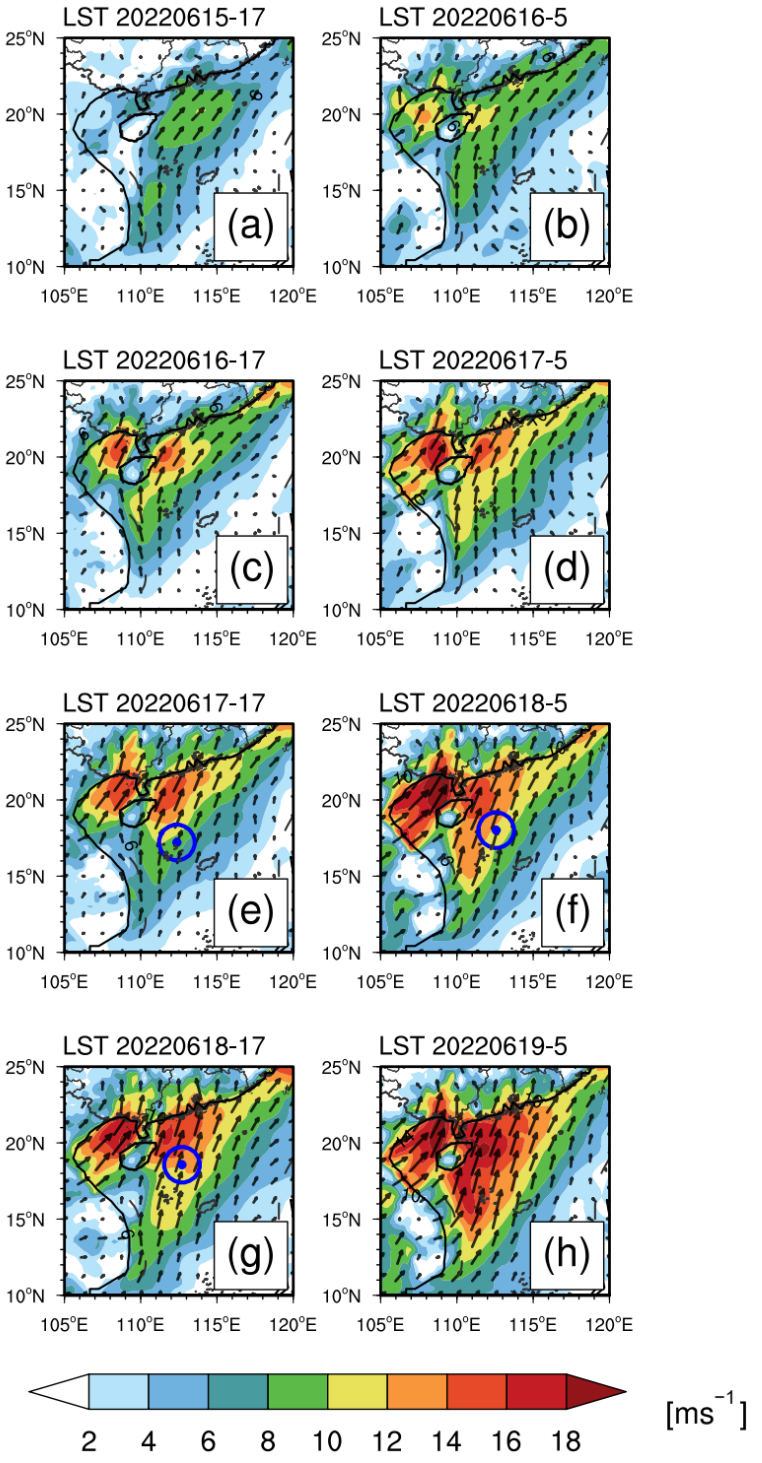

Figure 7. (a–h) Horizontal distributions of wind speeds (shading, m s^{-1}) and wind vectors at 950 hPa at twelve-hour intervals from 1700 LST on 15 June to 0500 LST 19 June. The blue markers indicate the locations of shipboard observations.

During the research period, the wind speeds at 950 hPa over the northern SCS exhibited a gradual strengthening trend on a synoptic scale, which was generally consistent with the results from the observation analysis. In the initial stage, the BLJ in the northern SCS had a width of approximately 4 degrees in longitude (110°E–114°E) and around 8 degrees in latitude (13°N–21°N). After intensification, the BLJ expanded to 9 degrees in longitude (109°E–118°E) and 14 degrees in latitude (10°N–24°N). On 15 June, the area with wind speed exceeding 10 m s^{-1} is very limited (Figure 7a), and the observed strong wind shear at this time is insufficient to meet the BLJ criterion. By 0500 LST on 16 June, the occurrence range of BLJs remains relatively small (Figure 7b), which explains why they were not detected in Figure 3b. As the overall wind strengthened, the width of the jet stream expanded from 2 degrees in longitude by 2 degrees in latitude to 5 degrees in longitude by 6 degrees in latitude by 1700 LST on 16 June (Figure 7c). The jet's rapid expansion along the latitude scale highlights the dominance of the southerly wind. From 17 to 18 June, the positions of the shipboard observations experienced minimal changes relative to BLJ regions (Figure 7e–g). In the observations, wind speeds at 950 hPa gradually increased during this period. By 0500 LST on 19 June, BLJs in northern SCS expanded to cover an area ranging between 12° to 22°N in latitude and 110° to 118°E in longitude (Figure 7h). Diurnally, BLJs in ERA5 were enhanced at night, with a peak around 0500 LST during the studied period.

The diurnal variations of BLJs are further compared among observation data and the ERA5 and MERRA2 datasets in Figure 8, with diurnal deviations calculated by subtracting their corresponding first-order linear trends in Figure 5. In the observational data, wind speeds reached their primary peak at 2300 LST, accompanied by a secondary peak at 1100 LST. Both the ERA5 and MERRA2 datasets struggled to accurately replicate the diurnal variation of BLJs observed. MERRA2 displayed an opposite pattern, with higher wind speeds during the daytime and lower wind speeds at nighttime. MERRA2's lower horizontal and temporal resolution makes it more difficult to capture the fine-scale variations and rapid changes within the boundary layer that influence BLJ characteristics. As a result, MERRA2 struggles to represent the diurnal variations of BLJs accurately, as these jets are influenced not only by synoptic-scale weather patterns but also by boundary layer processes. In contrast, ERA5 was able to capture the nighttime wind speed maxima, with the peak wind speed of BLJs occurring at 0500 LST and a secondary peak at 2300 LST. The anomaly peak at 0500 LST in ERA5 might be related to the 12 h windows used in the 4D-Var data assimilation of ERA5 at 0900 UTC and 2100 UTC [35], leading to sudden, artificial changes in diurnal variation at 0500 LST and 1700 LST (LST = UTC + 8) [43]. In summary, compared to MERRA2, the ERA5 dataset provided a slightly more accurate representation of the diurnal variations in wind speeds at 950 hPa during the observation period.

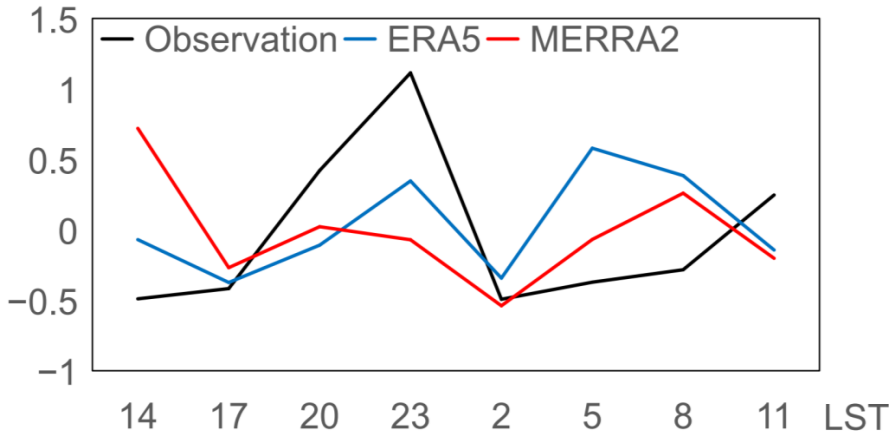

Figure 8. Diurnal variations of wind speed deviations at 950 hPa (m s^{-1}) averaged from June 15 to 18 in the observational data (black line), ERA5 (blue line), and MERRA2 (red line).

4.3. Quantitative Error Analysis

The FNL and JRA55 datasets are included to provide a broader comparison in the quantitative error analysis of reanalysis datasets (Figure 9). To calculate RMSEs and MAEs, wind speeds corresponding to the observation times were derived from the nearest raster points of the FNL, ERA5, JRA55, and MERRA2 datasets. Missing values caused by the six-hour temporal resolution of the FNL and JRA55 datasets were removed before the confidence intervals were calculated.

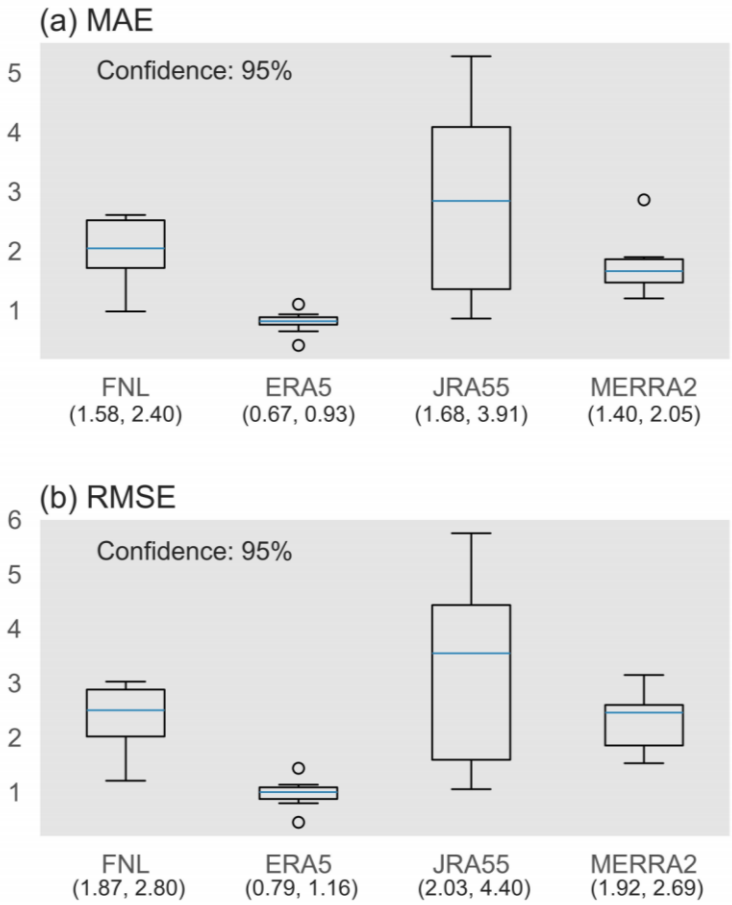

Figure 9. Box plots of (**a**) mean absolute errors (MAEs) and (**b**) root mean square errors (RMSEs) of wind speeds at 950 hPa across four reanalysis datasets: FNL, ERA5, JRA55, and MERRA2. The format of "(x1, x2)" below the names of the datasets represents the 95% confidence interval.

Among the datasets, ERA5 yielded the lowest and narrowest confidence interval in MAE (0.79–1.16 m s^{-1}) and RMSE (0.67–0.93 m s^{-1}), indicating the highest accuracy in reflecting observational data on a synoptic scale. During the enhancement period of the BLJ from 15 to 18 June, ERA5 exhibited more reliable performance in capturing the strength of BLJs, with both RMSE and MAE being less than 1.2 m s^{-1}. Overall, MERRA2 performed well, with relatively narrow confidence intervals for MAE and RMSE in the ranges of 1.40–2.05 and 1.90–2.69 m s^{-1}, respectively, surpassing all other datasets except ERA5. FNL and JRA55 exhibited poorer performance, with differences between the maximum and minimum confidence interval values in RMSEs of 0.93 and 1.97 m s^{-1}, respectively, particularly with JRA55 exceeding 4 m s^{-1} in this period. The wide range of the confidence interval suggests the need for further investigation and analysis to better understand the underlying data and reduce uncertainty. This degradation in performance might be attributed to their lower spatio-temporal resolutions.

To further examine the differences between the datasets, we conducted significance tests on the RMSEs and MAEs (Table 1). All three datasets—FNL, JRA55, and MERRA2—

passed the significance test at the 0.01 level when compared with ERA5, indicating significant differences from the ERA5 data. This finding supports the reliability of ERA5 shown in Figure 9. In contrast, the performance of JRA55 in Figure 9 exhibits distinct differences from the other datasets, which have achieved significance at the 0.01 level in the significance test. This suggests that JRA55, to a certain degree, lacks the capability to adequately characterize the BLJs in the northern SCS region during this observational period.

Table 1. The values of the average mean absolute error (MAE) and root mean square error (RMSE) between every two datasets among FNL, ERA5, JRA55, and MERRA2, along with the results of their significance tests.

MAE/RMSE	FNL	ERA5	JRA55	MERRA2
FNL	-	1.193 */1.360 *	−0.795/−0.882	0.266/0.028
ERA5	-	-	−1.994 */−2.242 *	−0.927 */−1.333 *
JRA55	-	-	-	1.067 */0.909 *
MERRA2	-	-	-	-

The values in the table are in the format of "MAE/RMSE", representing differences in the mean values of MAE and RMSE, respectively, rounded to three decimal places. The values marked with * indicate passing the significance test at the 0.01 level.

5. Environmental Conditions and Precipitation Associated with BLJs

This section explores the environmental conditions, potential mechanism for strengthening, and precipitation associated with BLJs using ERA5 and CMORPH data.

5.1. Environmental Conditions and Potential Maintenance Mechanism

The observed BLJs were located on the northwest side of a high-pressure system, associated with WPSH (Figure 10). The high-pressure system, characterized by geopotential heights exceeding 1520 gpm at 850 hPa, moved eastward across the SCS from 15 to 18 June. During this period, an enhanced low-pressure vortex in northwestern China also developed.

On 15 June, the high-pressure system covered part of the northern SCS, with the BLJ occurring along its northwestern edge (Figure 10a). From 16 to 18 June, the high-pressure system continued to retreat eastward, with the area of geopotential height above 1520 gpm moving out of the northern SCS (Figure 10b–d). Simultaneously, the low-pressure vortex significantly intensified, with the lowest geopotential height dropping to approximately 1400 gpm and shifting southward from around 35°N to South China. This shifting contributed to the enhancement of BLJ wind speeds due to the strengthening pressure gradient force between the high-pressure system over the sea and the strong low-pressure vortex over the mainland of China.

A momentum budget analysis based on the ERA5 dataset, depicted in Figure 11, was conducted to assess the factors influencing the temporal variations in wind speeds at 950 hPa from 15 to 18 June in the observation region (red box in Figure 1c). Since the magnitudes of the HAD and VAD terms were relatively small and could be neglected, the focus was placed on other terms.

On a synoptic scale, the meridional wind shows a continuous enhancement, whereas the zonal wind exhibits less pronounced variations. The negative zonal PGF term, which represents southerly geostrophic winds, decreased from -1 m s^{-1} h^{-1} to -2 m s^{-1} h^{-1} during this period. This decrease in zonal PGF indicates an intensification of the zonal pressure gradient force and the associated southerly geostrophic winds. Meanwhile, the meridional PGF term exhibited a subtle increase during 15–18 June. However, the zonal wind component did not show a corresponding slight enhancement on a synoptic scale, probably due to the contribution of ageostrophic winds.

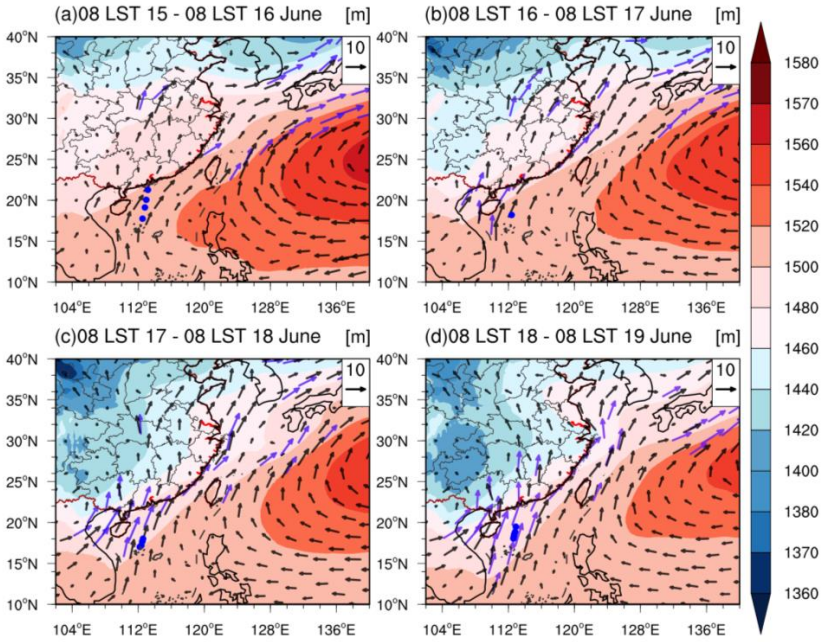

Figure 10. Horizontal distributions of daily averaged geopotential height at 850 hPa (shadings, gpm) and wind vectors (purple vectors indicate wind speeds greater than 10 m s^{-1}) at 950 hPa from (**a**–**d**) 15–18 June starting from 0800 LST. The blue markers indicate the locations of shipboard observations.

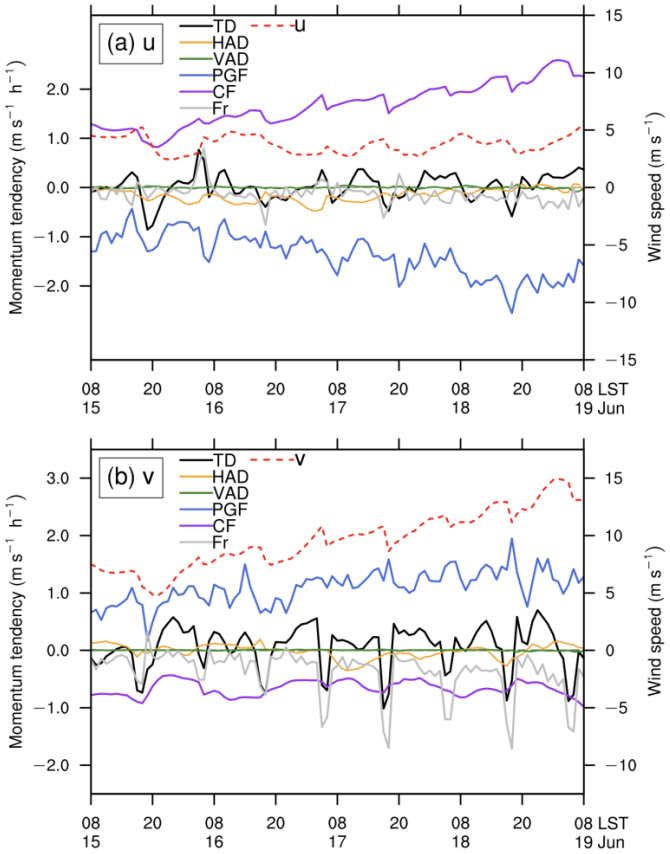

Figure 11. Temporal evolutions of momentum budget components at 950 hPa for the (**a**) zonal and (**b**) meridional winds, including the tendency term (TD, black line), horizontal advection (HAD, orange

line), vertical advection (VAD, green line), pressure gradient force (PGF, blue line), Coriolis force (CF, purple line), and the residual (friction, Fr, grey line). The red dashed lines indicate the zonal and meridional wind components in (**a**) and (**b**), respectively.

In terms of the temporal evolution of the geostrophic and ageostrophic wind components, the geostrophic wind showed a trend and magnitude more aligned with the total wind, while the ageostrophic wind exhibited more pronounced diurnal variations.

Furthermore, the horizontal distributions of pressure gradient force and corresponding geostrophic wind at 950 hPa are examined to understand the roles of pressure gradient force in strengthening BLJs on a synoptic scale (Figure 12). On 15 June, as the high-pressure system expanded over the northern SCS, the total pressure gradient force reached 0.2×10^{-3} m s^{-2}, and the geostrophic wind near Hainan Island attained 8 m s^{-1} (Figure 12a). On 16 June, the pressure gradient force experienced a slight intensification to 0.4×10^{-3} m s^{-2}, with stronger geostrophic wind across the northern SCS (Figure 12b). However, as the research vessel moved away from the core regions of BLJs, especially in the early morning of 16 June, a decrease in wind speeds was observed, as shown in Figure 3e. During 17–18 June, the low-pressure vortex intensified and extended southward. This shift led to a significant strengthening in the pressure gradient force to approximately 1×10^{-3} m s^{-2} and further caused the geostrophic wind to increase beyond 8 m s^{-1} in the northern SCS (Figure 12c,d). This increase in the pressure gradient force and geostrophic wind highlights the role of the low-pressure vortex in enhancing BLJs during this period.

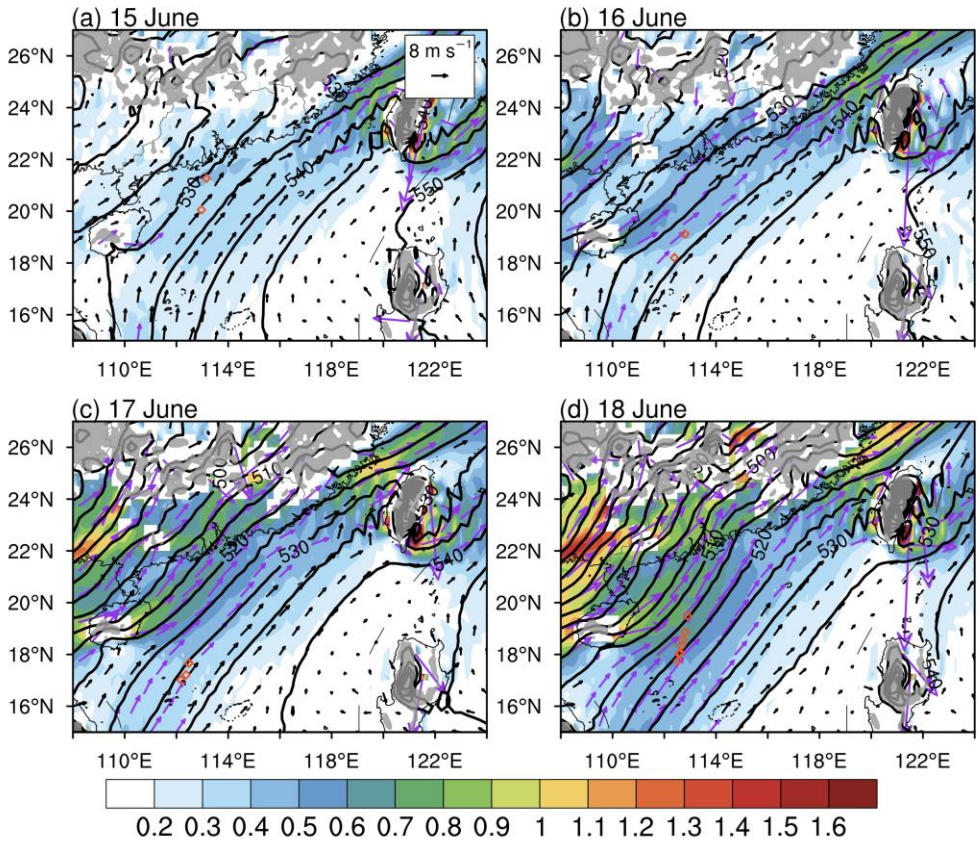

Figure 12. Horizontal distributions of daily averaged total pressure gradient force (shadings, 10^{-3} m s^{-2}), geostrophic wind (purple vectors indicate wind speed greater than 8 m s^{-1}), and geopotential height (contours, interval: 5 gpm) at 950 hPa on (**a**–**d**) 15–18 June, respectively. The red markers denote the positions of shipboard observations.

5.2. Precipitation Associated with BLJ

During the observation period, the location and intensity of precipitation over South China were significantly influenced by the BLJs in the northern SCS (Figure 13).

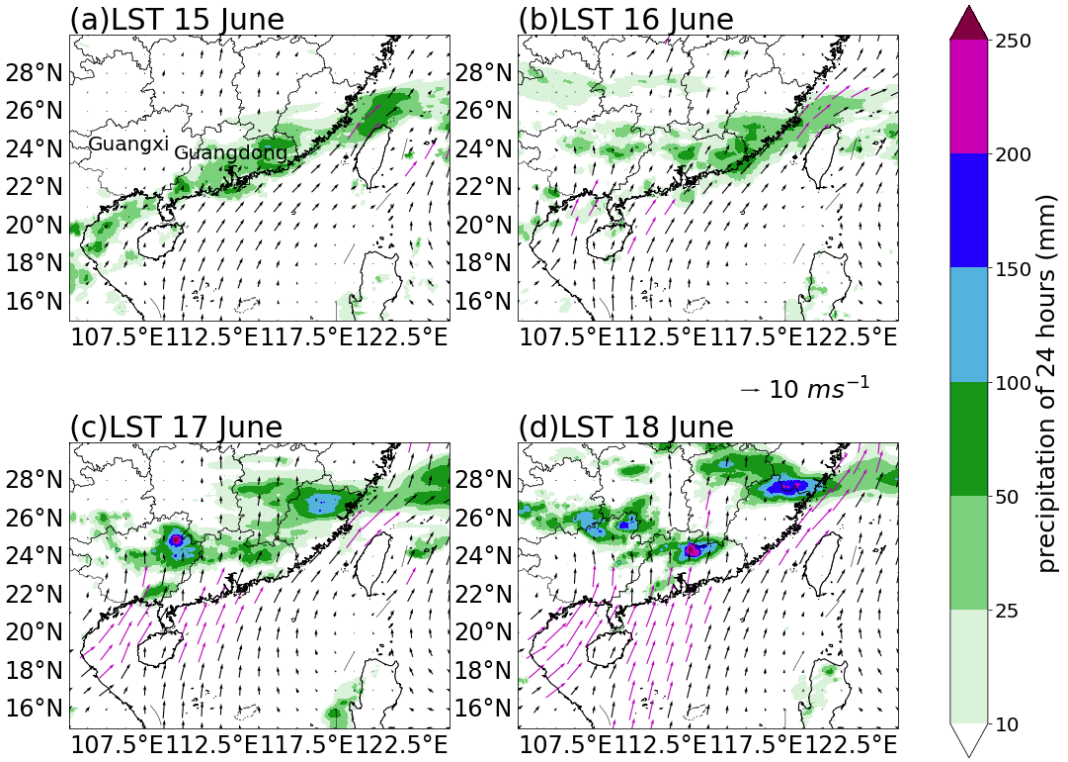

Figure 13. Horizontal distributions of accumulated 24 h precipitation (shadings, mm) starting from 0800 LST and daily average wind vectors (purple vectors indicate wind speeds greater than 10 m s^{-1}) on (**a**–**d**) 15–18 June.

On 15 June, heavy rainfall exceeding 50 mm day^{-1} was primarily concentrated in the coastal region of Guangdong Province, while a relatively weak BLJ was located on the eastern side of the Indochina Peninsula (Figure 13a). By 16 June, the rainband shifted northward, accompanied by the BLJ intensifying to exceed 10 m s^{-1} and moving northward towards the east of Hainan Island (Figure 13b).

During 17–18 June, there was a notable increase in precipitation intensity, corresponding with the significant strengthening southerly winds of the BLJs (Figure 13c,d). On 17 June, northern Guangxi Province experienced more than 250 mm day^{-1} of precipitation, coinciding with intensified BLJs in the Beibu Gulf. As the rainfall center moved eastward to Guangdong Province on 18 June, South China recorded more than 250 mm of 24 h cumulative precipitation, which is classified as an extreme rainstorm by the China Meteorological Administration. In summary, as the BLJs in the northern SCS strengthened during the observation period, the precipitation progressively moved northward from the coastline to the inland regions, reflecting the impact of the BLJs on rainfall distribution.

6. Summary and Conclusions

Boundary layer jets (BLJs), with jet cores lower than 900 hPa, frequently occur in the northern South China Sea (SCS) and significantly contribute to rainfall in South China. Despite their importance, direct observations of BLJs in this maritime region remain critically scarce. This study examines the characteristics and temporal evolutions of BLJs through direct observational data collected during a research voyage campaign from 15 to

18 June 2022. Additionally, it evaluates the performance of various reanalysis datasets in representing these BLJs during the observation period.

The observational campaign over northern SCS from 15 to 18 June 2022 coincided with an active period of BLJs, providing valuable insights into their detailed structures. The observation period is representative of typical conditions over the northern SCS, as its horizontal wind distribution and diurnal variation closely align with those observed in long-term reanalysis data [15,16]. Radiosonde data, obtained from soundings launched on the research vessel, indicated that BLJs primarily peaked at altitudes of 500–750 m above sea level. Synoptically, BLJ wind speeds exhibited a slight decrease from 15 to 16 June, followed by a significant increase after 17 June. Notably, on 17 June, double wind speed peaks were observed below 1 km, manifesting at altitudes of 250 and 700 m, respectively. Diurnally, BLJs exhibited peak wind speeds at 2300 LST and a secondary peak at 1100 LST. Temporal evolutions of moisture and wind speeds in the BLJs demonstrated similar trends, with an initial slight decrease in specific humidity followed by an increase in the thickness of the moisture layer.

This study also provides a detailed evaluation of the performances of ERA5 and MERRA2 reanalysis datasets in representing BLJs. On a synoptic scale, ERA5 effectively captured the weak decrease trend in wind speeds on 15 June and the subsequent BLJ enhancement on June 18. In contrast, MERRA2 performed poorly during 15–16 June but demonstrated improvement during the BLJ intensification period on 17–18 June. ERA5 generally underestimated specific humidity within the boundary layer while overestimating moisture at mid-levels around 800 hPa. Among the reanalysis datasets (ERA5, MERRA2, FNL, and JRA55), ERA5 demonstrated the best performance in representing BLJs on the synoptic scale, followed by MERRA2. However, both ERA5 and MERRA2 struggled to capture diurnal peaks in wind speeds, with ERA5 performing better in representing nocturnal wind speed acceleration.

During this period, the BLJs were enhanced by a substantial pressure gradient force, resulting from the high-pressure system over the ocean and a low-pressure vortex over inland regions, further promoting rainfall in South China. On 15 June, a high-pressure system covered part of the northern SCS, modestly enhancing geostrophic wind. From 16 to 18 June, a low-pressure vortex intensified and moved southward to South China, accompanied by the sustained eastward movement of the high-pressure system. The core regions of the BLJs were located between the low-pressure system inland and the high-pressure system over the sea. In addition, the positions and intensity of the BLJs significantly influenced precipitation in South China, with a northward movement to inland regions and intensification of the rainband on 17–18 June.

This study is significant as it provides rare observational data and evaluates the ability of reanalysis datasets to represent BLJs over the northern SCS. Direct observations, as precise measurements at specific locations, offer greater reliability and reduce uncertainties compared to reanalysis or satellite data, which are influenced by model assumptions and retrieval errors. Moreover, direct observations have the advantage of revealing fine-scale features and local variations. The observed double jet cores below 1 km were not captured by reanalysis datasets, likely due to their limited vertical and horizontal resolution as well as the boundary layer parameterization scheme.

In addition, ERA5 exhibits insufficient accuracy in the diurnal variation of BLJs compared to observation data. Given the potential for artificial discontinuities introduced by assimilation windows, ERA5 may be more suitable for synoptic-scale studies rather than resolving fine-scale diurnal variations in representing BLJs. Given that numerous studies have utilized reanalysis data to investigate BLJs, the comparison of four reanalysis datasets with observation data provides valuable insights for refining these datasets in the future.

Compared to other coastal BLJs that have been included in global statistical analyses, the BLJs in the northern SCS have been extensively documented through various case studies and regional analyses, highlighting their dependence on synoptic-scale systems as well as local thermal and dynamical processes [2,13,15]. The BLJs in the northern SCS

exhibit similar altitudes and wind speeds to other coastal BLJs, while they display unique diurnal variations. Unlike the typical single nocturnal peak observed in other coastal BLJs, driven by nocturnal boundary layer inversions, the BLJs in the northern SCS often exhibit double peaks diurnally, with one peak occurring during the nighttime and another in the afternoon.

To better understand the climatological characteristics of BLJs in the northern SCS, future research requires longer time series and higher-resolution observation data, potentially through repeated observations by scientific research vessels or intensive observations of fixed islands and reefs. The universality and inter-annual variation of BLJs before and after the onset of the SCS monsoon merit further investigation. Moreover, to improve the evaluation of reanalysis datasets, it is crucial to explore the specific weather conditions under which these datasets can more accurately reflect BLJ characteristics. In addition, other factors contributing to errors in these datasets warrant further investigation.

Author Contributions: Conceptualization, Y.D., X.Z. and Y.L.; methodology, X.Z. and Y.L.; software, X.Z. and Y.L.; validation, X.Z. and Y.L.; writing—original draft preparation, X.Z. and Y.L.; writing—review and editing, X.Z., Y.L. and Y.D.; visualization, X.Z. and Y.L.; supervision, Y.D.; project administration, Y.D.; funding acquisition, Y.D. All authors have read and agreed to the published version of the manuscript.

Funding: This study was supported by the National Natural Science Foundation of China (No. 42122033, 42075006, 42475002), the Innovation Group Project of Southern Marine Science and Engineering Guangdong Laboratory (Zhuhai) (No. 316323005), and the Key Innovation Team of China Meteorological Administration (CMA2023ZD08). We also acknowledge the high-performance computing support from the School of Atmospheric Science of Sun Yat-sen University.

Data Availability Statement: Publicly available reanalysis datasets were analyzed in this study. JRA55 data can be downloaded from Japanese 55-year Reanalysis, Daily 3-Hourly and 6-Hourly Data (https://rda.ucar.edu/datasets/ds628.0/dataaccess/# (accessed on 15–18 June 2022)). FNL data can be downloaded from NCEP FNL Operational Model Global Tropospheric Analyses, continuing from July 1999 (https://rda.ucar.edu/datasets/ds083.2/ (accessed on 15–18 June 2022)). MERRA2 data can be downloaded from Modern-Era Retrospective Analysis for Research and Applications, Version 2 (https://gmao.gsfc.nasa.gov/reanalysis/MERRA-2/; accessed on 15–18 June 2022). ERA5 data can be downloaded from the hourly data on pressure levels from 1940 to the present (https://cds.climate.copernicus.eu/; accessed on 15–18 June 2022). CMORPH data are available from the Climate Prediction Center morphing technique (https://www.ncei.noaa.gov/data/cmorph-high-resolution-global-precipitation-estimates/access/30min/8km/; accessed on 15–18 June 2022). The observational data can be downloaded online from Observational data in the maiden voyage of the Sun Yat-sen University Research Vessel (zenodo.org) (https://zenodo.org/records/13329759 (accessed on 15–18 June 2022)). This dataset encompasses a comprehensive range of parameters, sequentially detailing elapsed time, ascension rate, height above mean sea level, atmospheric pressure, ambient temperature, relative humidity, dew point temperature, wind direction, and wind speed.

Conflicts of Interest: The authors declare no conflicts of interest.

References

1. Stensrud, D.J. Importance of Low-Level Jets to Climate: A Review. *J. Clim.* **1996**, *9*, 1698–1711. [CrossRef]
2. Du, Y.; Chen, G. Climatology of Low-Level Jets and Their Impact on Rainfall over Southern China during the Early-Summer Rainy Season. *J. Clim.* **2019**, *32*, 8813–8833. [CrossRef]
3. Zhang, M.; Meng, Z. Warm-Sector Heavy Rainfall in Southern China and Its WRF Simulation Evaluation: A Low-Level-Jet Perspective. *Mon. Weather. Rev.* **2019**, *147*, 4461–4480. [CrossRef]
4. Du, S.; Wang, D.; Li, G.; Cai, Q.; Xu, X. Analyses of the Vertical Structure of Precipitation in South China based on Dual-Frequency Spaceborne Precipitation Radar GPM Product. *J. Trop. Meteorol.* **2020**, *36*, 115–130. [CrossRef]
5. Liu, H.; He, M.; Wang, B.; Zhang, Q. Advances in Low-Level Jet Research and Future Prospects. *Acta Meteorol. Sin.* **2014**, *28*, 57–75. [CrossRef]
6. Ling, G. Comparing Water Vapor Transport during Precipitation Processes in the Pre-Flood Period of South China and Precipitation Processes of Typhoons in the Post-Flood Period of South China: A Case Study. *Dyn. Atmos. Ocean.* **2023**, *102*, 101371. [CrossRef]

7. Zhao, P.; Sun, J.; Zhou, X. Mechanism of Formation of Low Level Jets in the South China Sea during Spring and Summer of 1998. *Chin. Sci. Bull.* **2003**, *48*, 1265–1270. [CrossRef]
8. Sun, J. A Study of the Basic Features and Mechanism of Boundary Layer Jet in Beijing Area. *Chin. J. Atmos. Sci.* **2005**, *29*, 445–452. [CrossRef]
9. Chen, Y.-L.; Chen, X.A.; Zhang, Y.-X. A Diagnostic Study of the Low-Level Jet during TAMEX IOP 5. *Mon. Weather Rev.* **1994**, *122*, 2257–2284. [CrossRef]
10. Du, Y.; Zhang, Q.; Ying, Y.; Yang, Y. Characteristics of Low-Level Jets in Shanghai during the 2008-2009 Warm Seasons as Inferred from Wind Profiler Radar Data. *J. Meteorol. Soc. Jpn. Ser. II* **2012**, *90*, 891–903. [CrossRef]
11. Du, Y.; Chen, G. Heavy Rainfall Associated with Double Low-Level Jets over Southern China. Part I: Ensemble-Based Analysis. *Mon. Weather Rev.* **2018**, *146*, 3827–3844. [CrossRef]
12. Du, Y.; Chen, G. Heavy Rainfall Associated with Double Low-Level Jets over Southern China. Part II: Convection Initiation. *Mon. Weather Rev.* **2019**, *147*, 543–565. [CrossRef]
13. Li, X.; Du, Y. Statistical Relationships between Two Types of Heavy Rainfall and Low-Level Jets in South China. *J. Clim.* **2021**, *34*, 8549–8566. [CrossRef]
14. Zhao, Y. Numerical Investigation of a Localized Extremely Heavy Rainfall Event in Complex Topographic Area during Midsummer. *Atmos. Res.* **2012**, *113*, 22–39. [CrossRef]
15. Dong, F.; Zhi, X.; Zhang, L.; Ye, C. Diurnal Variations of Coastal Boundary Layer Jets over the Northern South China Sea and Their Impacts on Diurnal Cycle of Rainfall over Southern China during the Early-Summer Rainy Season. *Mon. Weather Rev.* **2021**, *149*, 3341–3363. [CrossRef]
16. Du, Y.; Shen, Y.; Chen, G. Influence of Coastal Marine Boundary Layer Jets on Rainfall in South China. *Adv. Atmos. Sci.* **2022**, *39*, 782–801. [CrossRef]
17. Du, Y.; Chen, G.; Han, B.; Mai, C.; Bai, L.; Li, M. Convection Initiation and Growth at the Coast of South China. Part I: Effect of the Marine Boundary Layer Jet. *Mon. Weather Rev.* **2020**, *148*, 3847–3869. [CrossRef]
18. Luo, Y.; Du, Y. The Roles of Low-Level Jets in "21·7" Henan Extremely Persistent Heavy Rainfall Event. *Adv. Atmos. Sci.* **2023**, *40*, 350–373. [CrossRef]
19. Miao, Y.; Guo, J.; Liu, S.; Wei, W.; Zhang, G.; Lin, Y.; Zhai, P. The Climatology of Low-Level Jet in Beijing and Guangzhou, China. *JGR Atmos.* **2018**, *123*, 2816–2830. [CrossRef]
20. Liu, X.; Chen, G.; Zhang, S.; Du, Y. Formation of Low-Level Jets over Southern China in the Mei-Yu Season. *Adv. Atmos. Sci.* **2023**, *40*, 1731–1748. [CrossRef]
21. Blackadar, A.K. Boundary Layer Wind Maxima and Their Significance for the Growth of Nocturnal Inversions. *Bull. Am. Meteorol. Soc.* **1957**, *38*, 283–290. [CrossRef]
22. Li, J.; Chen, Y.-L. Barrier Jets during TAMEX. *Mon. Weather Rev.* **1998**, *126*, 959–971. [CrossRef]
23. Lin, P.-L.; Chen, Y.-L.; Chen, C.-S.; Liu, C.-L.; Chen, C.-Y. Numerical Experiments Investigating the Orographic Effects on a Heavy Rainfall Event over the Northwestern Coast of Taiwan during TAMEX IOP 13. *Meteorol. Atmos. Phys.* **2011**, *114*, 35. [CrossRef]
24. Du, Y.; Rotunno, R. A Simple Analytical Model of the Nocturnal Low-Level Jet over the Great Plains of the United States. *J. Atmos. Sci.* **2014**, *71*, 3674–3683. [CrossRef]
25. Du, Y.; Rotunno, R.; Zhang, Q. Analysis of WRF-Simulated Diurnal Boundary Layer Winds in Eastern China Using a Simple 1D Model. *J. Atmos. Sci.* **2015**, *72*, 714–727. [CrossRef]
26. Yan, Y.; Cai, X.; Wang, X.; Miao, Y.; Song, Y. Low-Level Jet Climatology of China Derived From Long-Term Radiosonde Observations. *JGR Atmos.* **2021**, *126*, e2021JD035323. [CrossRef]
27. Cui, C.; Zhou, W.; Yang, H.; Wang, X.; Deng, Y.; Wang, X.; Xu, G.; Wang, J. Analysis of the Characteristics of the Low-Level Jets in the Middle Reaches of the Yangtze River during the Mei-Yu Season. *Adv. Atmos. Sci.* **2023**, *40*, 711–724. [CrossRef]
28. Holt, T.; Sethuraman, S. Aircraft and Ship Observations of the Mean Structure of the Marine Boundary Layer over the Arabian Sea during MONEX 79. *Bound. Layer Meteorol.* **1985**, *33*, 259–282. [CrossRef]
29. Andreas, E.L.; Claffy, K.J.; Makshtas, A.P. Low-Level Atmospheric Jets And Inversions Over The Western Weddell Sea. *Bound. Layer Meteorol.* **2000**, *97*, 459–486. [CrossRef]
30. Jakobson, L.; Vihma, T.; Jakobson, E.; Palo, T.; Männik, A.; Jaagus, J. Low-Level Jet Characteristics over the Arctic Ocean in Spring and Summer. *Atmos. Chem. Phys.* **2013**, *13*, 11089–11099. [CrossRef]
31. Rubio, H.; Kühn, M.; Gottschall, J. Evaluation of Low-Level Jets in the Southern Baltic Sea: A Comparison between Ship-Based Lidar Observational Data and Numerical Models. *Wind Energy Sci.* **2022**, *7*, 2433–2455. [CrossRef]
32. Fan, W.; Liu, Y.; Chappell, A.; Dong, L.; Xu, R.; Ekström, M.; Fu, T.-M.; Zeng, Z. Evaluation of Global Reanalysis Land Surface Wind Speed Trends to Support Wind Energy Development Using In Situ Observations. *J. Appl. Meteorol. Climatol.* **2021**, *60*, 33–50. [CrossRef]
33. Gualtieri, G. Analysing the Uncertainties of Reanalysis Data Used for Wind Resource Assessment: A Critical Review. *Renew. Sustain. Energy Rev.* **2022**, *167*, 112741. [CrossRef]
34. Kalverla, P.C.; Duncan, J.B.; Steeneveld, G.-J.; Holtslag, A.A.M. Low-Level Jets over the North Sea Based on ERA5 and Observations: Together They Do Better. *Wind Energy Sci.* **2019**, *4*, 193–209. [CrossRef]
35. Hersbach, H.; Bell, B.; Berrisford, P.; Hirahara, S.; Horányi, A.; Muñoz-Sabater, J.; Nicolas, J.; Peubey, C.; Radu, R.; Schepers, D.; et al. The ERA5 Global Reanalysis. *Q. J. R. Meteorol. Soc.* **2020**, *146*, 1999–2049. [CrossRef]

36. Zeng, W.; Chen, G.; Du, Y.; Wen, Z. Diurnal Variations of Low-Level Winds and Precipitation Response to Large-Scale Circulations during a Heavy Rainfall Event. *Mon. Weather Rev.* **2019**, *147*, 3981–4004. [CrossRef]
37. Khosravi, K.; Shahabi, H.; Pham, B.T.; Adamowski, J.; Shirzadi, A.; Pradhan, B.; Dou, J.; Ly, H.-B.; Gróf, G.; Ho, H.L.; et al. A Comparative Assessment of Flood Susceptibility Modeling Using Multi-Criteria Decision-Making Analysis and Machine Learning Methods. *J. Hydrol.* **2019**, *573*, 311–323. [CrossRef]
38. Maier, H.R.; Jain, A.; Dandy, G.C.; Sudheer, K.P. Methods Used for the Development of Neural Networks for the Prediction of Water Resource Variables in River Systems: Current Status and Future Directions. *Environ. Model. Softw.* **2010**, *25*, 891–909. [CrossRef]
39. Karunasingha, D.S.K. Root Mean Square Error or Mean Absolute Error? Use Their Ratio as Well. *Inf. Sci.* **2022**, *585*, 609–629. [CrossRef]
40. Du, Y.; Chen, Y.-L.; Zhang, Q. Numerical Simulations of the Boundary Layer Jet off the Southeastern Coast of China. *Mon. Weather Rev.* **2015**, *143*, 1212–1231. [CrossRef]
41. Xue, M.; Luo, X.; Zhu, K.; Sun, Z.; Fei, J. The Controlling Role of Boundary Layer Inertial Oscillations in Meiyu Frontal Precipitation and Its Diurnal Cycles Over China. *JGR Atmos.* **2018**, *123*, 5090–5115. [CrossRef]
42. Shen, Y.; Du, Y. Sensitivity of Boundary Layer Parameterization Schemes in a Marine Boundary Layer Jet and Associated Precipitation during a Coastal Warm-Sector Heavy Rainfall Event. *Front. Earth Sci.* **2023**, *10*, 1085136. [CrossRef]
43. Chen, G.; Du, Y.; Wen, Z. Seasonal, Interannual, and Interdecadal Variations of the East Asian Summer Monsoon: A Diurnal-Cycle Perspective. *J. Clim.* **2021**, *34*, 4403–4421. [CrossRef]